

# Oxidation of Monolayer WS<sub>2</sub> in Ambient is a Photoinduced Process.

*Jimmy C. Kotsakidis<sup>1</sup>\*, Quanhui Zhang<sup>2</sup>, Amadeo L. Vazquez de Parga<sup>3,4</sup>, Marc Currie<sup>5</sup>,  
Kristian Helmerson<sup>1</sup>, D. Kurt Gaskell<sup>5</sup>, Michael S. Fuhrer<sup>1\*</sup>*

<sup>1</sup> *School of Physics and Astronomy, Monash University, Victoria 3800, Australia.*

<sup>2</sup> *Department of Civil Engineering, Monash University, Victoria 3800, Australia.*

<sup>3</sup> *Dep. Física de la Materia Condensada and Condensed Matter Physics Center (IFIMAC),  
Universidad*

*Autónoma de Madrid, Cantoblanco 28049, Madrid, Spain.*

<sup>4</sup> *IMDEA Nanociencia, Cantoblanco 28049, Madrid, Spain.*

<sup>5</sup> *U.S. Naval Research Laboratory, Washington D.C. 20375, USA.*

\*Address correspondence to [Michael.Fuhrer@monash.edu](mailto:Michael.Fuhrer@monash.edu) or [Jimmy.Kotsakidis@monash.edu](mailto:Jimmy.Kotsakidis@monash.edu)

Keywords: Transition metal dichalcogenides, Tungsten disulfide, Ambient air oxidation, Photo-oxidation, Defects, Monolayer.

## Abstract

We have studied the ambient air oxidation of chemical vapor deposition (CVD) grown monolayers of the semiconducting transition metal dichalcogenide (S-TMD)  $WS_2$  using optical microscopy, laser scanning confocal microscopy (LSCM), photoluminescence (PL) spectroscopy, and atomic force microscopy (AFM). Monolayer  $WS_2$  exposed to ambient conditions in the presence of light (typical laboratory ambient light for weeks, or typical PL spectroscopy map), exhibits damage due to oxidation which can be detected with the LSCM and AFM; though may not be evident in conventional optical microscopy due to poorer contrast and resolution. Additionally, this oxidation was not random, and correlated with ‘high-symmetry’ and red-shifted areas in the PL spectroscopy map – areas thought to contain a higher concentration of sulfur vacancies. In contrast, samples kept in ambient and darkness showed no signs of oxidation for up to 10 months. Low-irradiance/fluence experiments showed that samples subjected to excitation energies at or above the trion excitation energy (532 nm/2.33 eV and 660 nm/1.88 eV) oxidized, even for irradiances and fluences eight and four orders of magnitude lower (respectively) than previously reported. No significant oxidation was observed for 760 nm/1.63 eV light exposure, which lies below the trion excitation energy in  $WS_2$ . The strong wavelength dependence and apparent lack of irradiance dependence suggests that ambient oxidation of  $WS_2$  is initiated by photon-mediated electronic band transitions, that is, photo-oxidation. These findings have important implications for prior, present and future studies concerning direct bandgap S-TMDs measured, stored or manipulated in ambient conditions.

Since the discovery of two-dimensional (2D) van der Waals materials such as graphene<sup>1</sup> and the semiconducting transition metal dichalcogenides (S-TMDs),<sup>2</sup> 2D physics has become more accessible to laboratories around the world, leading to an exponential increase of published papers year upon year.<sup>3-4</sup> S-TMDs (and similarly graphene) possess radically different and useful properties in their 2D, monolayer form. Properties shared among some of the monolayer S-TMDs of family (Mo, W)(S, Se)<sub>2</sub> include a large direct bandgap,<sup>5-7</sup> exceptional optical characteristics<sup>8</sup> and strong spin-orbit coupling along with broken inversion symmetry.<sup>9</sup> This has lead various groups to demonstrate the usefulness of S-TMDs in potential applications ranging from ultra-low power electronics,<sup>10</sup> valley-tronics,<sup>11-12</sup> photonics<sup>13</sup> and qubits<sup>14</sup> to gas sensors.<sup>15</sup>

Understanding S-TMDs stability in ambient conditions and illumination by light – crucial for measurements and manipulations undertaken in those conditions – is essential for their development into potential applications. It is now well-known that monolayer and multilayer S-TMDs oxidize upon exposure to extreme conditions such as ultra-violet (UV) light irradiation in moisture-rich conditions<sup>16-17</sup> or elevated temperatures in ambient atmosphere.<sup>18-21</sup> More recently however, monolayer S-TMD oxidation has been reported in ambient conditions. For example, Gao *et al.*<sup>22</sup> were among the first to report that WS<sub>2</sub> and MoS<sub>2</sub> had poor long-term stability in ambient conditions and observe that H<sub>2</sub>O greatly sped up the oxidation process. Gao suggested the oxidation began with oxygen substitution at sulfur vacancy sites and continued via O or OH radicals, with H<sub>2</sub>O acting as a ‘catalyst’ lowering the energy barrier for reaction. In a subsequent report, Kang *et al.*<sup>23</sup> showed that oxidation was greatly suppressed, though not eliminated, when the S-TMD (in this case WS<sub>2</sub>) was epitaxially grown on graphene compared to an oxide substrate. It was proposed that electric fields were necessary for WS<sub>2</sub> oxidation, although the detailed

mechanism was unclear. Recently, Atkin *et al.*<sup>24</sup> determined that the oxidation reaction could be initiated by laser light (440 nm), and proposed a fluence threshold ( $>1.5 \times 10^{10} \text{ J m}^{-2}$ ) necessary for oxidation. Atkin also found that H<sub>2</sub>O was necessary for the oxidation reaction to proceed at any measurable rate (in agreement with Gao),<sup>22</sup> and in addition, found that sulfate was a likely reaction product.<sup>24</sup> Although these studies have identified important factors in the oxidation process *i.e.* ambient conditions, humidity, substrate, reaction products and radiant exposure levels – a complete and fundamental understanding of the conditions under which oxidation takes place, and more critically the conditions that completely avoid oxidation, is lacking.

In this work, we investigated ambient-exposed monolayers of the S-TMD WS<sub>2</sub> using standard characterization tools – optical microscopy, photoluminescence (PL) spectroscopy and atomic force microscopy (AFM). Moreover, we also employed laser scanning confocal microscopy (LSCM), which served as an integral tool to this work. By correlating AFM images with LSCM images, we are able to rapidly identify oxidized regions of monolayer WS<sub>2</sub>, which may not be evident from optical microscopy or PL spectroscopy. Oxidation is evident in samples kept in ambient conditions and exposed to light characteristic of laboratory conditions (typical room light for weeks), or moderate laser powers in PL mapping spectroscopy, but is not seen in as-grown samples or those stored in ambient conditions and darkness for up to ten months. We further explored the role of light by irradiating monolayer WS<sub>2</sub> samples with low-irradiance, visible light at 532 nm, 660 nm, and 760 nm. For WS<sub>2</sub> samples exposed to 532 nm and 660 nm light (above the threshold necessary for electronic excitation), oxidation was observed, whereas, samples exposed to 760 nm light did not show appreciable oxidation (similar to those left in darkness). This indicates that oxidation in ambient conditions requires photo-excitation, *i.e.*, oxidation is a photo-

induced process, at odds with recent interpretations.<sup>22-24</sup> Furthermore, photo-induced oxidation occurred at irradiances and fluences of eight and four orders of magnitude (respectively) lower than the irradiance and fluence thresholds proposed in Ref. 24, suggesting that the threshold for oxidation is extraordinarily low or absent. To our knowledge, a photo-oxidation mechanism in ambient conditions has not been previously described in detail for any member of the S-TMD family of materials. The details of the oxidation reaction – likely Förster resonance energy transfer (FRET) and/or photo-catalysis involving redox reactions with H<sub>2</sub>O and O<sub>2</sub> – requires further study. However, we expect the ambient air photo-oxidation of other direct bandgap S-TMDs (such as MoS<sub>2</sub>) to occur similarly. These findings establish important protocols for all researchers seeking to avoid damaging S-TMDs via oxidation.

## Results

WS<sub>2</sub> is grown on c-sapphire (single side polished) in an atmospheric-pressure chemical vapor deposition (CVD) process, described previously,<sup>25</sup> using mixtures of argon/hydrogen with WO<sub>3</sub> and sulfur powder precursors (see Methods and Figure S1 in the Supplementary Materials section for details).

Figure 1a shows an LSCM micrograph of an as-grown monolayer WS<sub>2</sub> crystal, stored after growth in darkness for approximately one month, and exposed to laboratory and LSCM light for short durations before being stored again in darkness. Figure 1b shows LSCM and optical micrographs taken on a similarly grown sample after approximately 19 days of exposure to ambient atmosphere and typical laboratory room lighting. The LSCM image (left side of Fig. 1b) shows dark spots within the WS<sub>2</sub> crystal in Fig. 1b, although these are not apparent in Fig. 1a. These dark spots are

difficult or impossible to observe in the optical micrograph of the same crystal, shown on the right side of Fig. 1b. As discussed in more detail below, the dark spots correspond to the complete or partial oxidation of small ( $<0.5 \mu\text{m}$ ) regions of  $\text{WS}_2$  (*i.e.*  $\text{WO}_{3-x}$ ). This observation is consistent with recent reports on the ambient air oxidation of monolayer S-TMDs, which have observed samples oxidizing in months<sup>22</sup> to as little as weeks.<sup>23</sup> After the observation of dark spots/oxidation in Figure 1b, care was taken to not expose freshly grown samples to ambient UV light in the room, as this was thought to contribute to the oxidation of the  $\text{WS}_2$ .<sup>16-17</sup> Thus, freshly grown crystals were stored in darkness. To understand the optical properties of our CVD grown  $\text{WS}_2$  and to investigate whether this could provide reasons for the causes of this oxidation, samples were mapped using confocal PL spectroscopy ( $\mu\text{-PL}$ ). Figure 1c shows LSCM and optical micrographs of a monolayer  $\text{WS}_2$  crystal after performing  $\mu\text{-PL}$  of the sample, but otherwise the sample was protected from light, while Figure 1d shows a sister sample imaged with the LSCM after storage in darkness for 10 months. The conditions of the PL imaging (excitation wavelength 532 nm, power  $140 \mu\text{W}$ , irradiance  $\approx 6.9 \times 10^8 \text{ W m}^{-2}$ , with total fluence of  $\approx 1.8 \times 10^8 \text{ J m}^{-2}$ , see Methods for details) are similar to those routinely used for optical characterization of S-TMD crystals.<sup>26</sup> For the PL-exposed sample in Figure 1c, similar dark spots as in Figure 1b are evident with the LSCM micrographs, though are not obvious for the conventional optical micrograph shown on the right side of Figure 1c, while the standard sample, shown in Figure 1d, which remained in darkness appears pristine. (In Figure 1d, a bright spot in the middle of the  $\text{WS}_2$  is evident; we identify this feature as a crystal seed center or multi-layer  $\text{WS}_2$ , and not related with oxidation). The results imply that light can oxidize monolayer  $\text{WS}_2$ . Considering there are many reports using PL excitation conditions of S-TMDs on the same order of magnitude as that used in this report, the observation of oxidation after  $\mu\text{-PL}$  was unexpected. Moreover, since the LSCM uses light to

image the samples, it also carries a probability of oxidizing the  $\text{WS}_2$ . Thus, care was taken to ensure that the final step in the analysis was light exposure from the LSCM, and that sister samples (such as the one in Figure 1d) were used as standards to compare with the effects of any analysis/light exposure that was undertaken. Yet even after two subsequent LSCM exposures, no oxidation is observed, the details of which can be found in the Supplementary Information (Section 2, Figure S2). As will become clear, the advantages of LSCM characterization stem from its inherent operation at low incident fluence – much lower than those found in PL experiments, or under low-light illumination for days. The LSCM can operate in two modes, the first uses white light from an LED (optical micrographs in Figures 1b and 1c) and the second uses 405 nm light in a confocal laser scanning setup. In the case of the white light, the  $\text{WS}_2$  is subjected to an irradiance of  $\approx 1.6 \times 10^4 \text{ W m}^{-2}$  and fluence of  $\approx 1.6 \times 10^5 \text{ J m}^{-2}$  (for 10 second exposures at  $100\times$  magnification). In the case of the 405 nm light, the irradiance and fluence were  $\approx 1.3 \times 10^8 \text{ W m}^{-2}$ , and  $\approx 8.8 \times 10^4 \text{ J m}^{-2}$ , respectively (see methods for details).

Figures 2a-d show the results of  $\mu$ -PL on a different crystal contained on the same sample as in Figure 1c. Figure 2a shows the  $\mu$ -PL intensity distribution of the  $\text{WS}_2$  monolayer. It can be seen that the PL intensity on the edges is much brighter than that of the center, as is observed in many other reports.<sup>6, 24, 26-31</sup> Also, the  $\mu$ -PL shows a three-fold rotationally symmetric pattern, not only in the intensity map, but also mirrored in the map of the peak photon energy (relating to the location of the exciton) shown in Figure 2b, *i.e.*, the two correlate with each other.<sup>28</sup> Figure 2c shows a representative spectrum from the central region of the crystal, deconvolved as two Voigt<sup>32</sup> spectra identified as the exciton peak at approximately  $2.03 \pm 0.01 \text{ eV}$  and smaller trion peak at  $1.97 \pm 0.01 \text{ eV}$ . A representative spectrum from the edge of the crystal is shown in Figure 2d, and is similarly

deconvolved, showing the exciton peak at approximately  $1.96 \pm 0.01$  eV and trion peak at  $1.91 \pm 0.01$  eV. Figure 2c and 2d show the heterogeneity of the optical characteristics of CVD grown WS<sub>2</sub> crystal on sapphire: similar optical heterogeneity was seen in all other sample growths. After  $\mu$ -PL analysis, the sample was stored in darkness and then imaged with LSCM as shown in Figure 2e. Similar to Fig. 1c, the sample shows signs of oxidation, manifesting as small and aligned triangles, similar to those observed in previous reports using conventional microscopy.<sup>17, 22-23, 26</sup>

To better understand the oxidized regions seen with the LSCM, the same sample was then imaged with AFM in intermittent-contact mode, shown in Figures 2f-h. Figure 2f shows an overview of the sample, and the extent of the oxidation. AFM resolves more clearly the dark spots seen in LSCM as triangular ‘islands’. These triangular islands in S-TMDs have been observed before and identified as tungsten oxide in various oxidation states,  $WO_{3-x}$  ( $0 \leq x \leq 1$ ).<sup>17, 23-24, 26</sup> We see that upon comparison of the  $\mu$ -PL shown in Figures 2a and 2b and the after effects of oxidation seen in the LSCM and AFM micrographs of Figures 2e and 2f respectively, that the oxidation occurs more prevalently in some regions in a well-defined pattern – following the three-fold symmetric pattern of lines extending from the center towards the vertices of the triangular crystal. Also, significant oxidation can be seen outside these areas, for example in the region with red-shifted PL corresponding to the spectrum in Fig. 2d. The inset of Figure 2f shows the height of the central part of the crystal as  $\approx 0.5$  nm, with the very edge of the crystal higher than that of the central part by  $\approx 0.5$  nm (though can go above or below this value in other regions, see Supplementary Information section 4), with a width of  $\approx 0.32$  nm (see Supplementary Information Figure S5c). In some samples (from different growth runs), this edge was visible under the LSCM (see Supplementary Information Figure S4). This higher edge region correlates well to the increased

edge PL intensity of the  $\mu$ -PL map (Figure 2a), and thus we tentatively ascribe the bright edge in the PL spectrum to this physical feature. The increased PL brightness around the edges of monolayer S-TMDs has also been reported on by others,<sup>6, 24, 26-31</sup> and the effect is attributed to either differences in chemical composition on the edges of the crystal<sup>6, 26-30</sup> or to water intercalation at the edges of the S-TMDs.<sup>24, 31, 33</sup>

Figure 2g and 2h show higher-resolution AFM topography and phase images respectively, of the triangular oxidation island feature outlined by the dotted black box in Figure 2f. The AFM topography image in Figure 2g shows that these triangular oxidation islands are not holes (as suggested by the LSCM in Figure 2e) but raised in topography by  $\approx 1.14$  nm above the surrounding WS<sub>2</sub>; this is consistent with thicker WO<sub>3-x</sub> remaining as the reaction product (see Supplementary Information Section 3 for in-depth analysis of oxidation heights). The phase contrast between the oxidation island and WS<sub>2</sub> (Fig. 2h) also indicates that the oxidized area is a different material. Thin films of WO<sub>3-x</sub> have a much higher transmittance than WS<sub>2</sub> at visible wavelengths (see Supplementary Information for transmittance, reflectance and absorptance of monolayer WS<sub>2</sub>) explaining the dark (see-through to substrate) appearance of these regions under the LSCM.<sup>34</sup> It was observed that for some oxidation islands, there was a small (<60 nm), round, raised region in the middle of the oxidation island. This spot, seen more clearly with the enhanced contrast of the phase image in Figure 2h, suggests this feature is a liquid drop, and could result from the absorption of water by hygroscopic sulfur oxides (see Supplementary Information section 7).<sup>24</sup>

The experiments thus far imply that visible light with wavelengths as long as 532 nm can cause oxidation of WS<sub>2</sub> in ambient, at irradiances typically used for PL spectroscopy. To determine the

physical mechanism of WS<sub>2</sub> oxidation, controlled, low-irradiance light exposure experiments were conducted with monolayer WS<sub>2</sub> samples at three specific wavelengths. The experiments used two lasers at 532 nm (2.33 eV) and 660 nm (1.88 eV) (see Methods for details and Supplementary Information for laser spectra) and a halogen light (XGY-II) filtered at 760 nm (1.63 eV), with irradiances of approximately 3.8 W m<sup>-2</sup>, 14.2 W m<sup>-2</sup>, and 2.2 W m<sup>-2</sup>, respectively. Figure 3a shows the absorptance spectrum of the WS<sub>2</sub> monolayers at  $\approx$ 293K, determined via subtracting the measured transmission and reflectance spectra from the total light impinging on the sample (additional details in Methods). The absorptance spectrum is consistent with previous observations for monolayer WS<sub>2</sub><sup>35-37</sup> and shows features characteristic of the ‘A’ exciton at  $619\pm2$  nm (2.003 $\pm$ 0.006 eV) and ‘B’ exciton at  $516\pm2$  nm (2.403 $\pm$ 0.009 eV), which arise from excitonic transitions in the spin-orbit split bands at K/K’ points in the Brillouin zone. The observed spin-orbit splitting,  $\Delta_{\text{SO}}$ , of  $0.400\pm0.015$  eV is close to previously measured values.<sup>36</sup>

The corresponding wavelengths used in the controlled low-irradiance light exposure experiments are colored appropriately and superimposed on Figure 3a. The 532 nm light was chosen to mimic the conditions found in the PL experiment, the 660 nm light was chosen as it is at the edge of the absorption of WS<sub>2</sub> (excites mainly the trion) and 760 nm light which is not significantly absorbed by the WS<sub>2</sub> (*i.e.* photon induced electronic transitions are improbable). Light was shone constantly on the samples for 7 days in ambient atmosphere (ranging from  $\approx$ 40% to  $\approx$ 60% humidity) and they were subsequently imaged using the LSCM, giving a total fluence (un-corrected for absorptance) of  $2.3\times10^6$  J m<sup>-2</sup>,  $8.6\times10^6$  J m<sup>-2</sup> and  $1.3\times10^6$  J m<sup>-2</sup> for the 532 nm, 660 nm and 760 nm light, respectively. Note that these fluences are at least an order of magnitude larger than that of the LSCM.

Figures 3b-e show the samples after the 7 days of exposure to different wavelengths (b-d) or kept in darkness for two weeks (e) as imaged with the LSCM. In Figures 3b and 3c, small triangular islands on the edges and the interior of the WS<sub>2</sub> indicate that the 532 nm (b), and 660 nm (c) light caused oxidation of the crystals. Figure 3d shows the results of 760 nm light exposure; no significant amount of oxidation can be detected. All samples (including those in Figures 3b to 3d) were exposed to small amounts of ambient light while mounting/removing the samples from the optical setup (and CVD furnace) and loading/measuring the samples for analysis with the LSCM. Though as can be seen in Figure 3d, these brief ambient light exposures do not cause any obvious oxidation (as observed with the LSCM) compared to Figures 3b and 3c which are severely oxidized. Figure 3e shows an LSCM image of a control sample kept in darkness for two weeks after growth; no oxidation is evident.

## Discussion

We have identified for the first time that the previously observed<sup>22-24</sup> ambient oxidation of a monolayer S-TMD requires exposure to light that is able to excite electronic transitions within the WS<sub>2</sub> *i.e.* the physical mechanism is photo-oxidation. While heating of TMDs in ambient has been shown to cause oxidation in S-TMDs,<sup>18-22</sup> we can rule out heating as the cause of oxidation in our experiments, as we observe similar oxidation for long-time exposures at low-irradiance in Figures 3b and 3c, with irradiances approximately eight orders of magnitude lower than the high-irradiance PL exposure in Figures 1c and 2a-b. This means that irradiance is not an important factor for oxidation. In contrast, fluence does appear to be essential. Light exposure at 440 nm (2.82 eV) at

high fluence ( $>1.5 \times 10^{10} \text{ J m}^{-2}$ ) has been previously observed to cause oxidation of monolayer S-TMDs.<sup>24</sup> Here we find that lower photon energy light (down to the threshold for electronic excitation, 1.88 eV for 660 nm) is sufficient for oxidation, using a fluence of about 4 orders of magnitude lower ( $\approx 2.3 \times 10^6 \text{ J m}^{-2}$  in Fig. 3b) than previously reported. It should be noted here, that taking into account the absorptance of WS<sub>2</sub> (from Figure 3a), the irradiance absorbed by the WS<sub>2</sub> is 0.67 W m<sup>-2</sup>, 0.38 W m<sup>-2</sup> and approximately zero for the 532 nm, 660 nm and 760 nm light respectively. Thus, the actual amount of absorbed light (*i.e.* light that is able to excite electronic transitions) is lower by an order of magnitude (though the uncorrected values of irradiance and fluence are quoted here for direct comparison with literature). In comparison, the LSCM images, which show no obvious signs of oxidation, were obtained using fluences of  $\approx 8.8 \times 10^4 \text{ J m}^{-2}$ . These observations suggest that a fluence threshold for oxidation is either non-existent or extraordinarily low, and that oxidation will simply occur at a rate that is proportional to the fluence. Thus, depending on the resolution of the probe used, oxidation may not be observed, though still be present even with brief exposures at low fluence.

Furthermore, the fact that the threshold photon energy (wavelength) corresponds well to the energy (wavelength) threshold for electronic excitation, (excitation of the trion) strongly suggests that the oxidation occurs through a photo-excitation process, *i.e.* photo-oxidation. The detailed mechanism — likely Förster resonance energy transfer (FRET) and/or photo-catalysis reactions involving H<sub>2</sub>O and O<sub>2</sub> — requires further study (see Supplementary Information for further discussion). However, we expect the ambient air photo-oxidation of other direct bandgap S-TMDs (such as MoS<sub>2</sub>) to occur similarly due to very similar chemistry. The necessity for photo-excited carriers for oxidation also explains the protection from oxidation of monolayer S-TMDs placed on graphene:<sup>23</sup>

semi-metallic graphene efficiently quenches the photoexcited carriers through non-radiative recombination, thus greatly reducing the available excited carriers for chemical reaction via FRET and/or photo-catalysis.<sup>38</sup>

We observe that oxidation does not occur randomly across individual monolayer WS<sub>2</sub> crystals, but rather, shows a preference for regions running roughly from the centers to the vertices of triangular crystals, *i.e.* arranged with threefold rotational symmetry around the crystal centers (Figure 2e-f). The same threefold rotationally symmetric pattern is seen in the  $\mu$ -PL (Figure 2a-b) and has been observed in our group previously<sup>31</sup> and by other groups,<sup>26-30</sup> and this region has previously been shown to be preferentially oxidized under high-power laser irradiation.<sup>26</sup> Recent work counting individual defects using conductive AFM has demonstrated that this three-fold symmetric region has a higher defect density than surrounding areas of the single crystal.<sup>39</sup> It is now known that the most common structural defects present in S-TMDs are in the form of sulfur vacancies, and this is true (with the exception of atomic layer deposition grown samples)<sup>40</sup> whether the samples are exfoliated,<sup>41-42</sup> grown via chemical vapor transport (CVT)<sup>43</sup> or CVD.<sup>30, 39</sup> Thus, it is likely that sulfur vacancies nucleate the oxidative growth of WO<sub>3-x</sub> species. However, the mechanism behind the changes in PL intensity<sup>26-31</sup> and peak position<sup>28</sup> is unclear. In particular, some groups have considered strain to explain changes in PL, but have subsequently ruled out strain due to the persistence of the threefold symmetric pattern upon transfer of the crystal to another substrate, which is thought to relieve strain in as-grown crystals.<sup>26, 29</sup> Oxidation was also observed in a region in which the exciton (and trion) emission peak was red-shifted (see Figures 2a-c). It has recently been observed that short duration plasma treatments can increase defect density in WS<sub>2</sub>, creating a neutral exciton peak that is red-shifted in energy  $\approx 0.1$  eV below the ‘defect free’ neutral exciton

peak at  $\approx 2.03$  eV (see Figure 2c).<sup>32</sup> Moreover, high resolution transmission electron microscopy was performed and in conjunction with simulations, suggests that this red-shifted neutral exciton peak is due to single sulfur vacancies. It may be that our measured red-shifted peak has contributions from both the trion and a defected neutral exciton (due to sulfur vacancies), though confirmation of this can only be determined through further study. What is clear, is that our results indicate that the process of obtaining PL spectra in ambient conditions will necessarily form small oxide regions and hence, the analysis of the spectra could be affected by several associated mechanisms, for example, strain imparted to surrounding WS<sub>2</sub> developed during oxide formation.<sup>44</sup> Further work is needed, for example by performing PL in an inert environment or vacuum, to determine the effect of defected regions on PL without oxidation. Additional work is also needed to determine whether defects are necessary to initiate the oxidation, or whether it can proceed in a defect-free basal-plane of WS<sub>2</sub> in ambient with light exposure.

## Conclusion

Our work has shown that the physical mechanism that causes the oxidation of WS<sub>2</sub> in ambient conditions is a photoinduced *i.e.* photo-oxidation mechanism. Oxidation was observed to not occur randomly, but in three-fold symmetric areas (as defined by  $\mu$ -PL) and areas in which there was an observed red-shift in exciton emission. It is thought that these areas contain more defects in the form of sulfur vacancies, and so provide a starting point from which oxidation can proceed. The fluence threshold that begins this photo-oxidation is at least four orders of magnitude lower than previously thought,<sup>24</sup>  $<2.3 \times 10^6$  J m<sup>-2</sup>. Furthermore, photo-oxidation does not occur when the samples are exposed to similar fluences with wavelengths that are not absorbed appreciably, seen

with the low-irradiance light experiment using 760 nm. Further work may be needed to determine whether a non-zero radiant threshold for damage exists, as it is possible that oxidation has occurred in our lowest-exposure samples but is not yet detectable using e.g. LSCM or AFM, due to resolution limitations, or very low oxidation defect densities. Though taking into consideration that oxidation is only observed upon excitation of an electronic transition, it is likely that no threshold exists, and that oxidation occurs on a probabilistic basis. That is, lower light levels progress the reaction at much slower rates that are impossible to observe using optical microscopy. Still, our study already places severe constraints on the processing and analysis of S-TMD films in ambient conditions, since exposure to typical room light for extended periods, or exposure to a single typical scanning PL or Raman spectroscopy measurement may cause significant oxidative damage. Furthermore, we expect that these findings will guide the development of new nanofabrication techniques that completely prevent significant oxidation of S-TMDs, as the storage of S-TMDs in darkness or exposure to light that cannot excite electronic transitions should completely prevent progression of the oxidation reaction.

## Methods

**Chemical Vapor Deposition.** An atmospheric-pressure CVD method was used to grow monolayer WS<sub>2</sub> on polished (single side) c-sapphire(0001) substrates (Shinkosha) in a 1-inch quartz tube furnace. The samples were determined to be monolayer from PL and AFM measurements, as presented in the main text. Before beginning the CVD process, the c-sapphire substrates were ultra-sonicated in acetone and ethanol, and then loaded into a 1-inch tube furnace in preparation for oxygen annealing. The samples were oxygen annealed by flowing oxygen at 50 sccm for at least 5 minutes over the sample after which the furnace was then ramped from 30 °C to 1050 °C in 30 minutes, held for 1 hour and then allowed to naturally cool to room temperature. After oxygen annealing, approximately 1.1 ±0.1 g of sulfur powder (≥99.5%, Sigma-Aldrich) and 2 ±0.1 g of WO<sub>3</sub> powder (≥99.9%, Sigma-Aldrich) were loaded in separate quartz boats. The sulfur was placed upstream and away from the central part of the furnace heating coils and under external heating coils (controlled by a separate temperature controller), while the WO<sub>3</sub> was loaded in the central part of the furnace along with the oxygen annealed substrates. A quartz test tube (approximately 22 mm in diameter) was placed against the substrate quartz boat, with the open

end facing outwards so as to restrict the flow of reactants (see Supplementary Fig. S1). This helps increase the partial pressure of reactants over the substrates, thus promoting growth of WS<sub>2</sub>. The furnace setup is illustrated in the supplementary material. Argon was used as the carrier gas and flowed at 200 sccm, and H<sub>2</sub> was also added to the gas stream at 8 sccm after purging with argon for 10 minutes. The furnace and external heating coils were then heated to approximately 900 °C and 200 °C from 30 °C in 30 minutes, respectively and held for approximately 5 minutes at these temperatures. After cooling to 800 °C, the furnace lid was opened slightly, so as to rapidly cool the furnace. Between 600 °C and 500 °C, the furnace was fully opened, and the H<sub>2</sub> gas turned off. The sulfur was allowed to naturally cool from 200 °C to room temperature. The samples were removed and immediately stored in containers wrapped with aluminum foil and stored in a toolbox.

**Photoluminescence spectroscopy.** Crystals were analyzed using a WITec 300R spectrometer equipped with a 532 nm laser and power set at approximately 140 μW (as judged by an optical power meter after the 100× objective). 2D confocal PL maps (μ-PL) were taken using the 100×/0.9 (Olympus MPLFLN) objective lens. A Gaussian beam profile was assumed, and the maximum irradiance estimated as  $I = 8P/(\pi D^2)$ , where  $P$  is the laser power and  $D$  is the diameter of the beam, estimated as  $D = 1.22\lambda/NA \approx 721$  nm, where  $\lambda$  is the wavelength in nanometers and  $NA$  is the numerical aperture of the lens. The μ-PL map shown in Figs. 2a and 2b took  $\approx 25$  minutes to complete (75×75 pixels,  $\approx 0.27$  seconds integration time per pixel). All PL measurements were taken at 20 °C ambient temperature and rel. humidity of 40 – 60%.

**Laser scanning confocal microscopy.** Two different LSCM's were used. In Fig 1b, a Keyence VK-X200 system was employed. In all other LSCM figures, an Olympus OLS4100 system was used. These microscopes are also able to take standard optical images, as shown juxtaposed in figures 1b and 1c in the main text, by use of a white LED. The white LED irradiance was calculated for the OLS4100 by first measuring the spectrum of the white LED, whose output was confined to the range 420 – 650 nm. A power meter was then used to measure the optical power exiting the 100×/0.95 objective lens. The responsivity of the power meter's silicon photodetector varies monotonically over this range of wavelengths; hence we were able to put bounds on the power measurement by calibrating the responsivity at two extrema of the spectrum, 420 nm and 650 nm. The power was found to be bounded by  $\approx 0.210 \pm 0.070$  mW. The field of view of the 100×/0.95 is 128 μm, and the irradiance was then calculated using  $I = 4P/(\pi D^2)$ . For the blue laser at 405 nm, a power meter measured the maximum output as  $\approx 14$  μW after the 100×/0.95 objective. The irradiance was then calculated assuming a Gaussian beam, similar to the photoluminescence setup. The time taken per scan varied depending on the magnification used, though the longest time of approximately 50 seconds (corresponding to un-zoomed 100x magnification) was used to calculate the fluence,  $H$ , in which case the irradiance was multiplied by the total exposure time for each pixel,  $t$ :  $H = 2Pt/(\pi r^2)$ . The exposure time was calculated by dividing the total time for the scan (50 seconds) by the total number of pixels (1024×1024). The laser beam diameter is much larger than a pixel, and so would result in the laser 'spilling over' to multiple pixels. To estimate this effect, the area of the laser beam was divided by the area of a pixel to give  $\approx 14$ . Thus, the calculated time was multiplied by 14 to estimate an upper limit to the true exposure time, yielding  $\approx 8.8 \times 10^4$  J m<sup>-2</sup>. A similar estimate is obtained by dividing the total energy delivered during the complete scan by the total area imaged.

**Atomic force microscopy.** A Bruker Dimension Icon AFM in tapping mode was used to obtain the atomic force micrographs. RTESPA-300 tips were used, and analysis was conducted using

WSxM v4.0.<sup>45</sup> In Figures 2f, 2g, 2h, the image was flattened, and the contrast enhanced. Bruker's own software was also used to analyze the height of the oxidized triangular islands (using the step height analysis function) and this data can be found in the Supplementary Information.

**Controlled low-light irradiance/fluence experiments.** Light sources were a 532 nm laser diode, 650 nm laser diode (measured to be 660 nm, see Supplementary Information) and halogen light source (XGY-II) with appropriate bandpass filter at 760 nm (Thorlabs FB760-10). The optical spectra of the laser sources can be found in the supplementary material. A custom-built enclosure was used to shroud the experiment in darkness. In the enclosure, the optics used were an iris (Thorlabs ID25), beam steering mirrors, a circular linear variable neutral density filter and a simple convex lens to expand the beam to an appropriate size. Samples were mounted onto a glass slide using double sided sticky tape. Standard samples (usually a sister sample from the same growth run), were kept in darkness for the entirety of the light exposure experiments. The irradiance and fluence for the sources were calculated similarly to the LSCM and PL sections above with the exception that the 760 nm light was assumed to be non-Gaussian (as in the white LED case with the LSCM), i.e  $I = 4P/(\pi D^2)$ . Values for the irradiance were calculated as  $3.8 \text{ W m}^{-2}$   $14.2 \text{ W m}^{-2}$  and  $2.2 \text{ W m}^{-2}$  for the 532 nm, 660 nm and 760 nm light respectively. Values for the fluence were then found by multiplying the irradiance by 604800 seconds (seconds in 7 days) to give  $2.3 \times 10^6 \text{ J m}^{-2}$ ,  $8.6 \times 10^6 \text{ J m}^{-2}$  and  $1.3 \times 10^6 \text{ J m}^{-2}$  for the 532 nm, 660 nm and 760 nm light respectively.

**Reflectance / Transmission / Absorptance Measurements and Calculations.** The reflectance and transmission spectra of the WS<sub>2</sub> monolayer crystals were measured over 350 – 800 nm using a Perkin Elmer Lambda 1050, equipped with an integrating sphere. Samples grown on c-sapphire (Shinkosha) were mounted on clear glass microscope slides (Sail). Blank sapphire substrates (Shinkosha) mounted on clear glass microscope slides (Sail) from the same batches were also measured. This allowed the absorptance from only the WS<sub>2</sub> to be determined and was done so in the following way. The absorptance of the substrates,  $A_s = 1 - T_s - R_s$ , was subtracted from the absorptance of the WS<sub>2</sub> and substrate, given as  $A_{ws2+s} = 1 - T_{ws2+s} - R_{ws2+s}$ , to yield the absorptance from only the WS<sub>2</sub> using the formula  $A_{ws2} = A_{ws2+s} - A_s = (T_s - T_{ws2+s}) + (R_s - R_{ws2+s})$ , where  $T_i$  and  $R_i$  are the measured transmittance and reflectance respectively of the substrate ( $i = S$ ) and WS<sub>2</sub> plus substrate ( $i = WS2+S$ ). The transmittance, reflectance and absorptance of the WS<sub>2</sub> on the substrate and the substrate itself are shown in the Supplementary Material.

## Associated Content

Supporting Information is available. Furnace setup is elucidated. The effects of multiple LSCM scans are visualized. Oxidation height analysis with AFM of triangular islands is presented. Details of the edges of WS<sub>2</sub> is analyzed further with LSCM and AFM. The spectra of the lasers used in the study are presented, and the transmittance reflectance and absorptance of the WS<sub>2</sub> on sapphire on glass and sapphire on glass are presented. Details of FRET and photo-catalysis are given, and possible reaction products relating to the microscopic features seen in Figure 2g-h are discussed. Finally a heating results of monolayer WS<sub>2</sub> (in the absence of light) is presented.

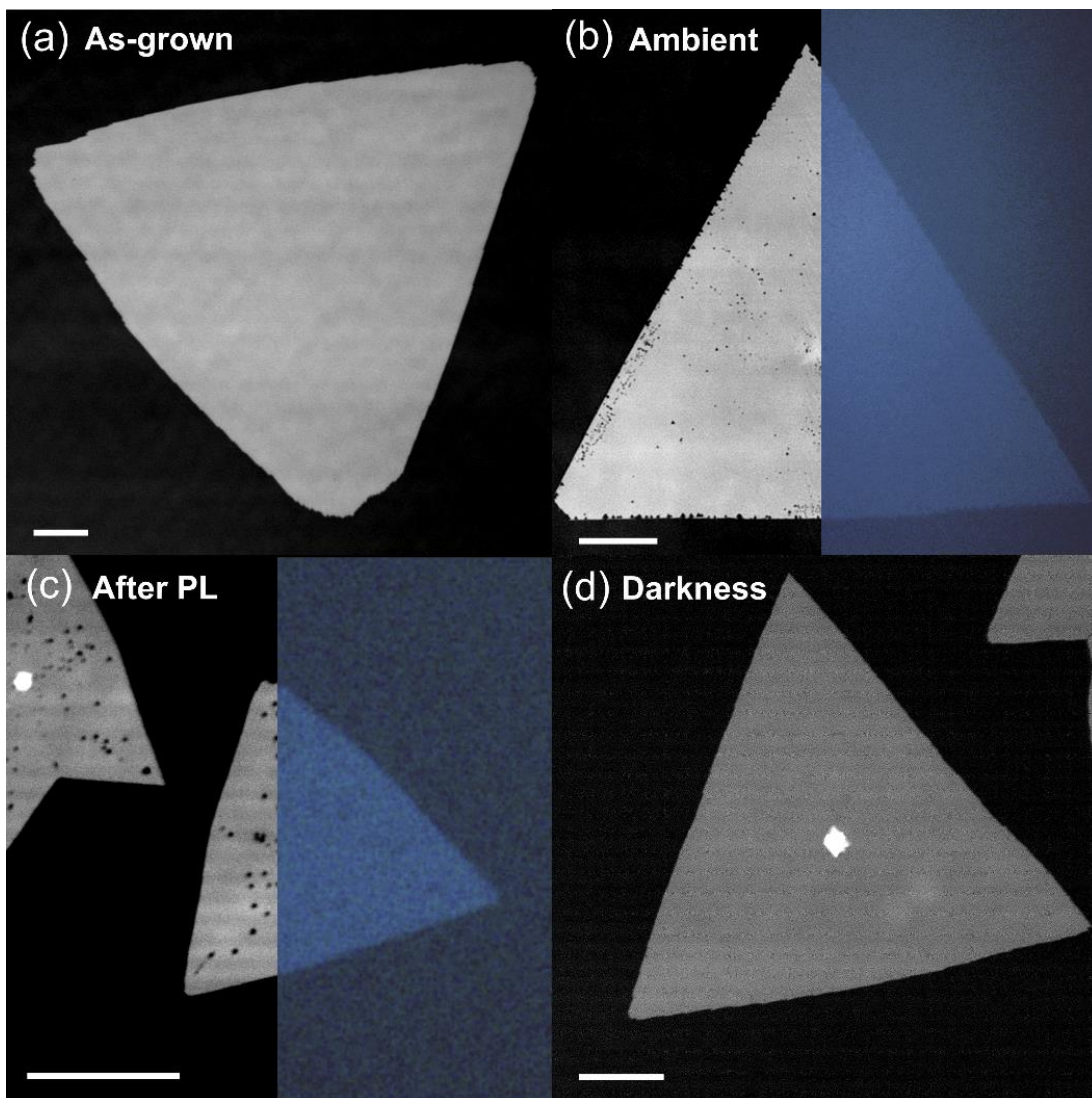


**Figure 1.** Laser scanning confocal micrograph of (a) CVD grown monolayer WS<sub>2</sub> exposed to minimal amounts of light before imaging with the LSCM approximately 1 month after growth. (b) WS<sub>2</sub> after approximately 19 days in ambient conditions, juxtaposed with an optical image of the same crystal. (c) WS<sub>2</sub> after routine photoluminescence spectroscopy, juxtaposed with an optical image of the same crystal and (d) WS<sub>2</sub> crystals kept in darkness for approximately 10 months, with brief exposure to ambient light. In the middle of this crystal is a crystal seed center, which was common throughout growths. Scale bars in all images are 10  $\mu\text{m}$ .

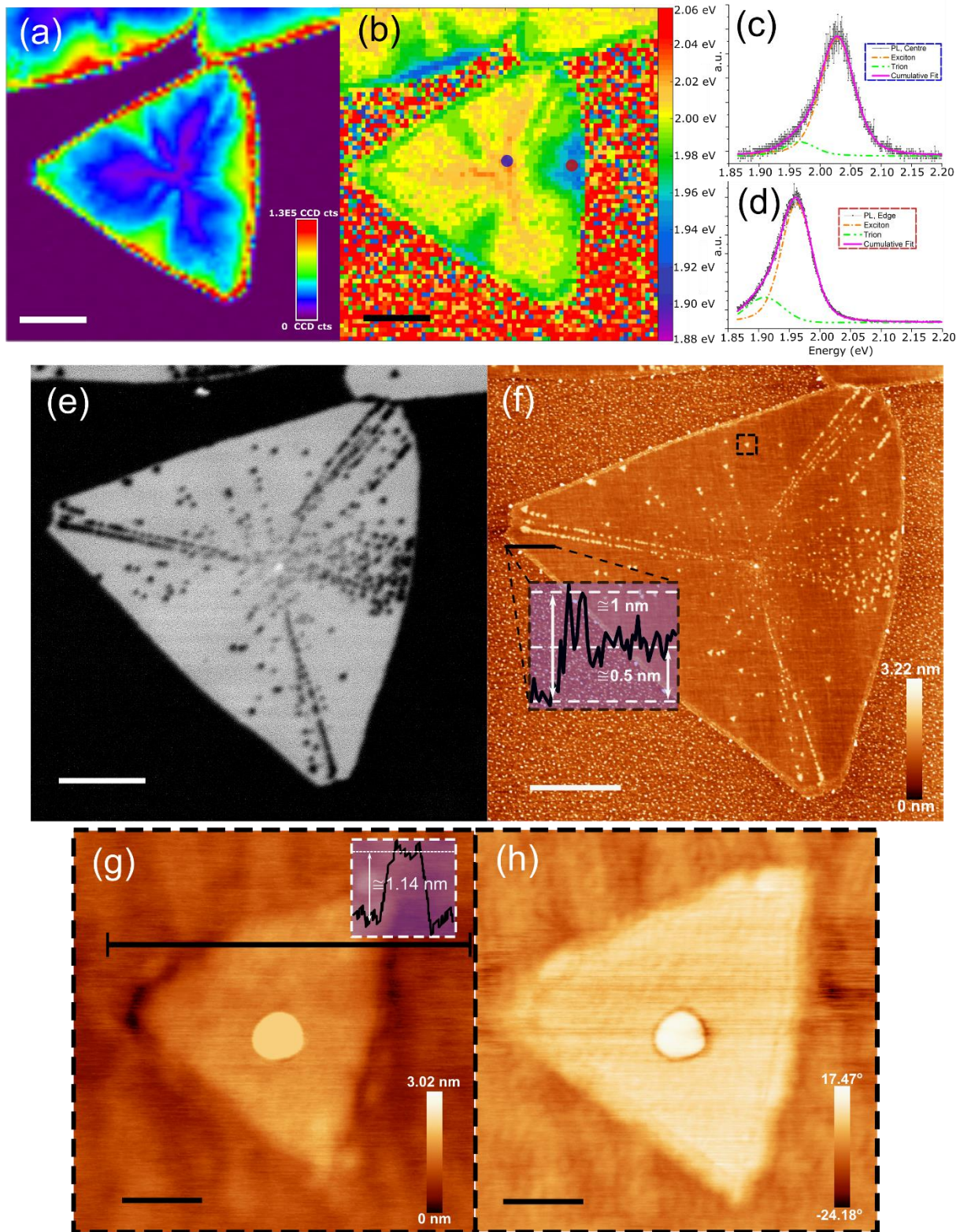


**Figure 2. (a), (b), (c), d)**  $\mu$ -PL of monolayer WS<sub>2</sub>. **(a)** Map showing the intensity in charged coupled device (CCD) counts (cts) (scale bar = 5  $\mu$ m) and **(b)** shows the approximate location of

the peak in intensity from (a) (scale bar = 5  $\mu\text{m}$ ). (c) shows the PL spectrum obtained from the central spot (blue) in (b) with exciton and trion peak energies at  $2.03\pm0.01$  and  $1.97\pm0.01$  eV respectively. (d) shows the PL spectrum from the edge region (red spot) with exciton and trion peak energies of  $1.96\pm0.01$  and  $1.91\pm0.01$  eV respectively. (e), (f) LSCM and AFM images showing oxidation of the same monolayer  $\text{WS}_2$  crystal in Figure 2, after analysis with  $\mu\text{-PL}$  (scale bars = 4  $\mu\text{m}$ ). In (e), an LSCM micrograph shows the oxidation as dark spots due to their altered transmittance. The morphology of these oxidation triangles was further investigated using AFM. In (f), the tapping mode AFM height micrograph shows unambiguously that these oxidation zones are raised, triangular and aligned along the stress/strain lines of the crystal. Inset shows the measured height of the crystal. (g), (h) Show a zoom in of the boxed area (scale bars = 65 nm) in (f) of a triangular oxidation island. The AFM phase image in (g), shows that the island is different in phase from the surrounding  $\text{WS}_2$ , and the AFM height image in (h) shows the height of this island is  $\approx 1.14$  nm (inset).

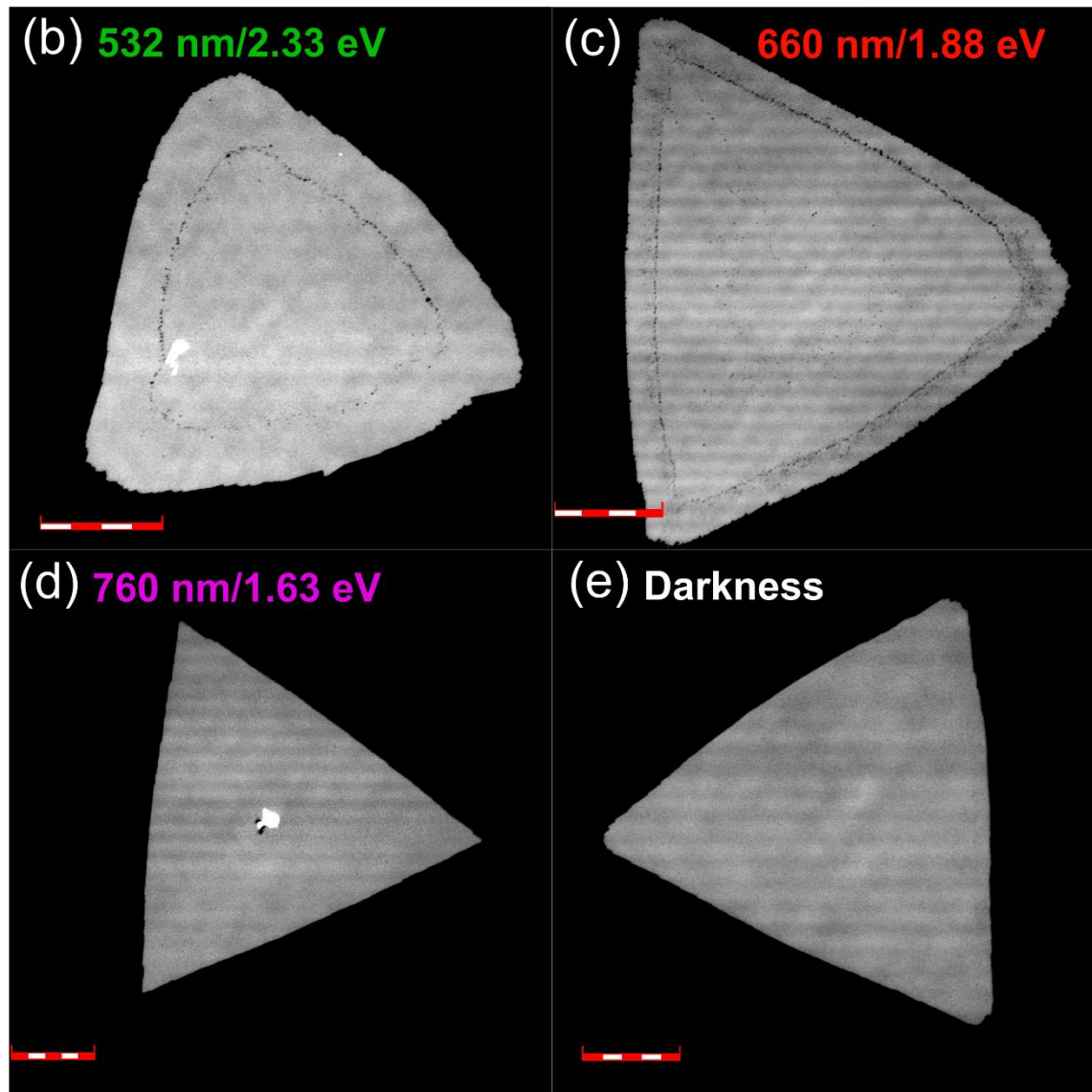
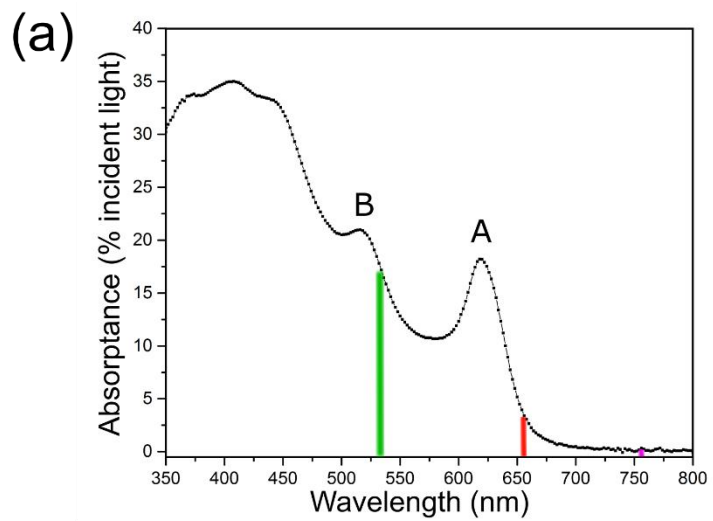


**Figure 3.** **(a)** Shows the absorbance spectrum of monolayer WS<sub>2</sub> taken at  $\approx$ 293K. Labels denote the ‘A’ exciton at  $619\pm 2$  nm ( $2.003\pm 0.006$  eV) and ‘B’ exciton at  $516\pm 2$  nm ( $2.403\pm 0.009$  eV). Color bands correspond to the wavelengths used for the low light exposure experiments, from left to right these are 532 nm (green), 660 nm (red) and 760 nm (pink). **(b),(c),(d)** Low-irradiance light exposure experiments. Laser scanning confocal micrographs of monolayer WS<sub>2</sub> after **(b)** 7 days exposure to green laser (532 nm/2.33 eV,  $4.2\text{ W m}^{-2}$ ) scale bar = 20  $\mu\text{m}$ , **(c)** 7 days of exposure to red light (650 nm/1.91 eV,  $14\text{ W m}^{-2}$ ) scale bar = 20  $\mu\text{m}$ , **(c)** 7 days of exposure to far-red light (760 nm/1.63 eV,  $2.2\text{ W m}^{-2}$ ) scale bar = 10  $\mu\text{m}$ . **(e)** A standard sample kept in darkness for 2 weeks for comparison with light exposed samples, scale bar = 10  $\mu\text{m}$ .

## AUTHOR INFORMATION

### Corresponding Authors

**\*Email (J. C. Kotsakidis): Jimmy.Kotsakidis@monash.edu**

**\*Email (M. S. Fuhrer): Michael.Fuhrer@monash.edu**

### Author Contributions

J.C.K and M.C made the first observation with the LSCM, which was later developed further by J.C.K with the help of D.K.G, M.S.F, A.L.V.P and Q.Z. J.C.K grew most of the samples, with some samples grown by Q.Z. AFM was conducted by J.C.K and Q.Z. PL was conducted by J.C.K. Low light irradiance/fluence laser experiments were conceived by J.C.K. and A.L.V. P and carried out by JCK. Optical absorptance/transmittance/reflectance was conducted by J.C.K and A.C. J.C.K wrote the manuscript with significant editorial contributions by M.S.F, D.K.G and A.L.V.P. The manuscript was written through contributions of all authors. All authors have given approval to the final version of the manuscript.

### Funding Sources

J.C.K and M.S.F acknowledge funding support from the Australian Research Council (DP150103837). D.K.G and M.C acknowledge funding from the Office of Naval Research (ONR). A.L.V.P acknowledges the Ministerio de Economía y Competitividad (MINECO) project FIS2015-67367-C2-1-P and Comunidad de Madrid project NMAT2D P2018/NMT-4511 for financial support. Q.Z. acknowledges funding support from the Australian Research Council (DE190101249).

### Notes

The authors declare no competing financial interests.

## ACKNOWLEDGMENT

J.C.K would like to thank A. Chesman for transmittance/reflectance/absorptance measurements, F. Shanks for use of the WITec PL/Raman system, as well as useful discussions, M. Greaves for time on the LSCM and S. Johnstone for assistance with equipment in the optical laboratory. J.C.K also acknowledges the hospitality of the U.S. Naval Research Laboratory (NRL) in which the initial investigations were performed. This work was performed in part at the Melbourne Centre for Nanofabrication (MCN) in the Victorian Node of the Australian National Fabrication Facility (ANFF).

## ABBREVIATIONS

CVD, Chemical Vapor Deposition; PL, Photoluminescence ;  $\mu$ -PL, confocal micro-photoluminescence (mapping) spectroscopy; LSCM, Laser scanning confocal microscope ; FRET, Förster Resonance Energy Transfer.

## References

1. Novoselov, K. S.; Geim, A. K.; Morozov, S. V.; Jiang, D.; Zhang, Y.; Dubonos, S. V.; Grigorieva, I. V.; Firsov, A. A., Electric Field Effect in Atomically Thin Carbon Films. *science* **2004**, *306* (5696), 666-669.
2. Novoselov, K.; Jiang, D.; Schedin, F.; Booth, T.; Khotkevich, V.; Morozov, S.; Geim, A., Two-Dimensional Atomic Crystals. *Proceedings of the National Academy of Sciences* **2005**, *102* (30), 10451-10453.
3. Randviir, E. P.; Brownson, D. A.; Banks, C. E., A Decade of Graphene Research: Production, Applications and Outlook. *Materials Today* **2014**, *17* (9), 426-432.
4. Choi, W.; Choudhary, N.; Han, G. H.; Park, J.; Akinwande, D.; Lee, Y. H., Recent Development of Two-Dimensional Transition Metal Dichalcogenides and Their Applications. *Materials Today* **2017**, *20* (3), 116-130.
5. Mak, K. F.; Lee, C.; Hone, J.; Shan, J.; Heinz, T. F., Atomically Thin MoS<sub>2</sub>: A New Direct-Gap Semiconductor. *Physical Review Letters* **2010**, *105* (13), 136805.
6. Gutiérrez, H. R.; Perea-López, N.; Elías, A. L.; Berkdemir, A.; Wang, B.; Lv, R.; López-Urías, F.; Crespi, V. H.; Terrones, H.; Terrones, M., Extraordinary Room-Temperature Photoluminescence in Triangular WS<sub>2</sub> Monolayers. *Nano Letters* **2012**, *13* (8), 3447-3454.
7. Tongay, S.; Zhou, J.; Ataca, C.; Lo, K.; Matthews, T. S.; Li, J.; Grossman, J. C.; Wu, J., Thermally Driven Crossover from Indirect Toward Direct Bandgap in 2D Semiconductors: MoSe<sub>2</sub> versus MoS<sub>2</sub>. *Nano Letters* **2012**, *12* (11), 5576-5580.
8. Dong, N.; Li, Y.; Feng, Y.; Zhang, S.; Zhang, X.; Chang, C.; Fan, J.; Zhang, L.; Wang, J., Optical Limiting and Theoretical Modelling of Layered Transition Metal Dichalcogenide Nanosheets. *Scientific Reports* **2015**, *5*, 14646.
9. Xiao, D.; Liu, G.-B.; Feng, W.; Xu, X.; Yao, W., Coupled Spin and Valley Physics in Monolayers of MoS<sub>2</sub> and other Group-VI Dichalcogenides. *Physical Review Letters* **2012**, *108* (19), 196802.
10. Fiori, G.; Bonaccorso, F.; Iannaccone, G.; Palacios, T.; Neumaier, D.; Seabaugh, A.; Banerjee, S. K.; Colombo, L., Electronics Based on Two-Dimensional Materials. *Nature Nanotechnology* **2014**, *9* (10), 768.
11. Zeng, H.; Dai, J.; Yao, W.; Xiao, D.; Cui, X., Valley Polarization in MoS<sub>2</sub> Monolayers by Optical Pumping. *Nature Nanotechnology* **2012**, *7* (8), 490.
12. Mak, K. F.; He, K.; Shan, J.; Heinz, T. F., Control of Valley Polarization in Monolayer MoS<sub>2</sub> by Optical Helicity. *Nature Nanotechnology* **2012**, *7* (8), 494.
13. Ye, Y.; Wong, Z. J.; Lu, X.; Ni, X.; Zhu, H.; Chen, X.; Wang, Y.; Zhang, X., Monolayer Excitonic Laser. *Nature Photonics* **2015**, *9* (11), 733.

14. Tran, T. T.; Choi, S.; Scott, J. A.; Xu, Z. Q.; Zheng, C.; Seniutinas, G.; Bendavid, A.; Fuhrer, M. S.; Toth, M.; Aharonovich, I., Room-Temperature Single-Photon Emission from Oxidized Tungsten Disulfide Multilayers. *Advanced Optical Materials* **2017**, *5* (5), 1600939.

15. Yang, W.; Gan, L.; Li, H.; Zhai, T., Two-Dimensional Layered Nanomaterials for Gas-Sensing Applications. *Inorganic Chemistry Frontiers* **2016**, *3* (4), 433-451.

16. Ly, T. H.; Chiu, M.-H.; Li, M.-Y.; Zhao, J.; Perello, D. J.; Cichocka, M. O.; Oh, H. M.; Chae, S. H.; Jeong, H. Y.; Yao, F., Observing Grain Boundaries in CVD-Grown Monolayer Transition Metal Dichalcogenides. *ACS Nano* **2014**, *8* (11), 11401-11408.

17. Yamamoto, M.; Dutta, S.; Aikawa, S.; Nakaharai, S.; Wakabayashi, K.; Fuhrer, M. S.; Ueno, K.; Tsukagoshi, K., Self-Limiting Layer-by-Layer Oxidation of Atomically Thin WSe<sub>2</sub>. *Nano Letters* **2015**, *15* (3), 2067-2073.

18. Rong, Y.; He, K.; Pacios, M.; Robertson, A. W.; Bhaskaran, H.; Warner, J. H., Controlled Preferential Oxidation of Grain Boundaries in Monolayer Tungsten Disulfide for Direct Optical Imaging. *ACS Nano* **2015**, *9* (4), 3695-3703.

19. Zhang, Y.; Zhang, Y.; Ji, Q.; Ju, J.; Yuan, H.; Shi, J.; Gao, T.; Ma, D.; Liu, M.; Chen, Y., Controlled Growth of High-Quality Monolayer WS<sub>2</sub> Layers on Sapphire and Imaging its Grain Boundary. *ACS Nano* **2013**, *7* (10), 8963-8971.

20. Yamamoto, M.; Einstein, T. L.; Fuhrer, M. S.; Cullen, W. G., Anisotropic Etching of Atomically Thin MoS<sub>2</sub>. *The Journal of Physical Chemistry C* **2013**, *117* (48), 25643-25649.

21. Wu, J.; Li, H.; Yin, Z.; Li, H.; Liu, J.; Cao, X.; Zhang, Q.; Zhang, H., Layer Thinning and Etching of Mechanically Exfoliated MoS<sub>2</sub> Nanosheets by Thermal Annealing in Air. *Small* **2013**, *9* (19), 3314-3319.

22. Gao, J.; Li, B.; Tan, J.; Chow, P.; Lu, T.-M.; Koratkar, N., Aging of Transition Metal Dichalcogenide Monolayers. *ACS Nano* **2016**, *10* (2), 2628-2635.

23. Kang, K.; Godin, K.; Kim, Y. D.; Fu, S.; Cha, W.; Hone, J.; Yang, E. H., Graphene-Assisted Antioxidation of Tungsten Disulfide Monolayers: Substrate and Electric-Field Effect. *Advanced Materials* **2017**, *29* (18), 1603898.

24. Atkin, P.; Lau, D.; Zhang, Q.; Zheng, C.; Berean, K.; Field, M.; Ou, J.; Cole, I.; Daeneke, T.; Kalantar-Zadeh, K., Laser Exposure Induced Alteration of WS<sub>2</sub> Monolayers in the Presence of Ambient Moisture. *2D Materials* **2017**, *5* (1), 015013.

25. Zhang, Q.; Lu, J.; Wang, Z.; Dai, Z.; Zhang, Y.; Huang, F.; Bao, Q.; Duan, W.; Fuhrer, M. S.; Zheng, C., Reliable Synthesis of Large-Area Monolayer WS<sub>2</sub> Single Crystals, Films, and Heterostructures with Extraordinary Photoluminescence Induced by Water Intercalation. *Advanced Optical Materials* **2018**, 1701347.

26. Sheng, Y.; Wang, X.; Fujisawa, K.; Ying, S.; Elias, A. L.; Lin, Z.; Xu, W.; Zhou, Y.; Korsunsky, A. M.; Bhaskaran, H., Photoluminescence Segmentation Within Individual

Hexagonal Monolayer Tungsten Disulfide Domains Grown by Chemical Vapor Deposition. *ACS Applied Materials & Interfaces* **2017**, 9 (17), 15005-15014.

27. Peimyoo, N.; Shang, J.; Cong, C.; Shen, X.; Wu, X.; Yeow, E. K.; Yu, T., Nonblinking, Intense Two-Dimensional Light Emitter: Monolayer WS<sub>2</sub> Triangles. *ACS Nano* **2013**, 7 (12), 10985-10994.
28. Chunxiao Cong, J. S., Xing Wu, Bingchen Cao, Namphung Peimyoo, Caiyu Qiu, Litao Sun, Ting Yu, Synthesis and Optical Properties of Large-Area Single-Crystalline 2D Semiconductor WS<sub>2</sub> Monolayer from Chemical Vapor Deposition. *Advanced Optical Materials* **2014**, 2 (2), 131-136.
29. McCreary, K. M.; Hanbicki, A. T.; Singh, S.; Kawakami, R. K.; Jernigan, G. G.; Ishigami, M.; Ng, A.; Brintlinger, T. H.; Stroud, R. M.; Jonker, B. T., The Effect of Preparation Conditions on Raman and Photoluminescence of Monolayer WS<sub>2</sub>. *Scientific Reports* **2016**, 6, 35154.
30. Liu, H.; Lu, J.; Ho, K.; Hu, Z.; Dang, Z.; Carvalho, A.; Tan, H. R.; Tok, E. S.; Sow, C. H., Fluorescence Concentric Triangles: A Case of Chemical Heterogeneity in WS<sub>2</sub> Atomic Monolayer. *Nano Letters* **2016**, 16 (9), 5559-5567.
31. Zhang, Q.; Chang, Z.; Xu, G.; Wang, Z.; Zhang, Y.; Xu, Z. Q.; Chen, S.; Bao, Q.; Liu, J. Z.; Mai, Y. W., Strain Relaxation of Monolayer WS<sub>2</sub> on Plastic Substrate. *Advanced Functional Materials* **2016**, 26 (47), 8707-8714.
32. Chow, P. K.; Jacobs-Gedrim, R. B.; Gao, J.; Lu, T.-M.; Yu, B.; Terrones, H.; Koratkar, N., Defect-Induced Photoluminescence in Monolayer Semiconducting Transition Metal Dichalcogenides. *ACS Nano* **2015**, 9 (2), 1520-1527.
33. Zheng, C.; Xu, Z.-Q.; Zhang, Q.; Edmonds, M. T.; Watanabe, K.; Taniguchi, T.; Bao, Q.; Fuhrer, M. S., Profound Effect of Substrate Hydroxylation and Hydration on Electronic and Optical Properties of Monolayer MoS<sub>2</sub>. *Nano Letters* **2015**, 15 (5), 3096-3102.
34. Song, C.; Chen, H.; Fan, Y.; Luo, J.; Guo, X.; Liu, X., High-Work-Function Transparent Conductive Oxides with Multilayer Films. *Applied Physics Express* **2012**, 5 (4), 041102.
35. Zhao, W.; Ghorannevis, Z.; Chu, L.; Toh, M.; Kloc, C.; Tan, P.-H.; Eda, G., Evolution of Electronic Structure in Atomically Thin Sheets of WS<sub>2</sub> and WSe<sub>2</sub>. *ACS Nano* **2012**, 7 (1), 791-797.
36. Hanbicki, A.; Currie, M.; Kioseoglou, G.; Friedman, A.; Jonker, B., Measurement of High Exciton Binding Energy in the Monolayer Transition-Metal Dichalcogenides WS<sub>2</sub> and WSe<sub>2</sub>. *Solid State Communications* **2015**, 203, 16-20.
37. Zhu, B.; Chen, X.; Cui, X., Exciton Binding Energy of Monolayer WS<sub>2</sub>. *Scientific Reports* **2015**, 5, 9218.

38. Froehlicher, G.; Lorchat, E.; Berciaud, S., Charge Versus Energy Transfer in Atomically Thin Graphene-Transition Metal Dichalcogenide van der Waals Heterostructures. *Physical Review X* **2018**, 8 (1), 011007.

39. Rosenberger, M. R.; Chuang, H.-J.; McCreary, K. M.; Li, C. H.; Jonker, B. T., Electrical Characterization of Discrete Defects and Impact of Defect Density on Photoluminescence in Monolayer WS<sub>2</sub>. *ACS Nano* **2018**, 12 (2), 1793-1800.

40. Hong, J.; Hu, Z.; Probert, M.; Li, K.; Lv, D.; Yang, X.; Gu, L.; Mao, N.; Feng, Q.; Xie, L., Exploring Atomic Defects in Molybdenum Disulphide Monolayers. *Nature Communications* **2015**, 6, 6293.

41. Addou, R.; Colombo, L.; Wallace, R. M., Surface Defects on Natural MoS<sub>2</sub>. *ACS Applied Materials & Interfaces* **2015**, 7 (22), 11921-11929.

42. Vancsó, P.; Magda, G. Z.; Pető, J.; Noh, J.-Y.; Kim, Y.-S.; Hwang, C.; Biró, L. P.; Tapasztó, L., The Intrinsic Defect Structure of Exfoliated MoS<sub>2</sub> Single Layers Revealed by Scanning Tunneling Microscopy. *Scientific Reports* **2016**, 6, 29726.

43. Edelberg, D.; Rhodes, D.; Kerelsky, A.; Kim, B.; Wang, J.; Zangiabadi, A.; Kim, C.; Abhinandan, A.; Ardelean, J.; Scully, M., Hundredfold Enhancement of Light Emission via Defect Control in Monolayer Transition-Metal Dichalcogenides. *arXiv:1805.00127* **2018**.

44. Conley, H. J.; Wang, B.; Ziegler, J. I.; Haglund Jr, R. F.; Pantelides, S. T.; Bolotin, K. I., Bandgap Engineering of Strained Monolayer and Bilayer MoS<sub>2</sub>. *Nano Letters* **2013**, 13 (8), 3626-3630.

45. Horcas, I.; Fernández, R.; Gomez-Rodriguez, J.; Colchero, J.; Gómez-Herrero, J.; Baro, A., WSXM: A Software for Scanning Probe Microscopy and a Tool for Nanotechnology. *Review of Scientific Instruments* **2007**, 78 (1), 013705.